Wettability-driven pore-filling instabilities
Microfluidic and numerical insights

Yan, Lifei; Müller, Johannes C.; van Noorden, Tycho L.; Weigand, Bernhard; Raoof, Amir

DOI
10.1016/j.jcis.2025.137884

Publication date
2025

Document Version
Final published version

Published in
Journal of Colloid and Interface Science

Journal of Colloid and Interface Science 696 (2025) 137884

Contents lists available at ScienceDirect

Journal of Colloid And Interface Science

journal homepage: www.elsevier.com/locate/jcis

Regular Article

Wettability-driven pore-filling instabilities: Microfluidic and numerical insights

Lifei Yan [a,b,1], Johannes C. Müller [c,*,1], Tycho L. van Noorden [d], Bernhard Weigand [c], Amir Raoof [b]

[a] Department of Earth Sciences, Utrecht University, Princetonlaan 8a, Utrecht, 3584 CB, Netherlands
[b] Faculty of Civil Engineering and Geosciences, Delft University of Technology, Stevinweg 1, Delft, 2628 CN, Netherlands
[c] Institute of Aerospace Thermodynamics, University of Stuttgart, Pfaffenwaldring 31, Stuttgart, D-70569, Germany
[d] COMSOL.BV, Röntgenlaan 37, Zoetermeer, 2719 DX, Netherlands

GRAPHICAL ABSTRACT

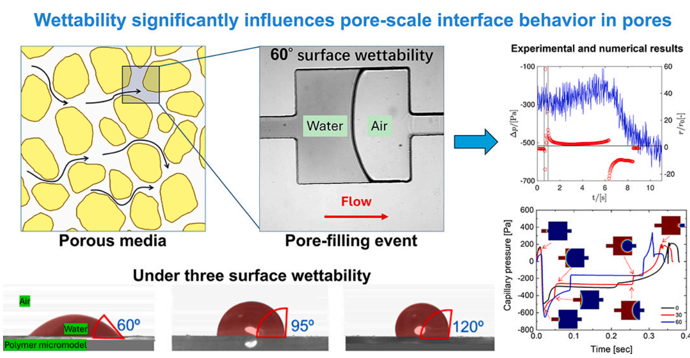

ARTICLE INFO

Dataset link: https://doi.org/10.18419/darus-4683

Keywords:
Wettability effect
Two-phase flow
Dynamic pore-filling
Pore-scale interface dynamics
Experimental and numerical validation

ABSTRACT

Hypothesis: Interface dynamics, such as Haines jumps, are crucial in multi-phase flow through porous media. However, the role of intrinsic surface wettability in pore-filling events remains unclear, and the pressure response requires further study. This work evaluates the impact of wettability on interface stability and pressure dynamics.
Experiments and simulations: We performed microfluidic experiments and level-set simulations of two-phase flow. Water displaced air or Fluorinert in a PDMS micro-model with controlled wettability (contact angles: 60°, 95°, 120°). Three injection velocities covered capillary- to viscous-dominated flow regimes. High-resolution imaging and synchronized pressure recordings linked interface curvature with capillary pressure changes.
Findings: At low capillary numbers, wettability strongly affects burst pressure and pinning. Its influence decreases at higher capillary numbers. We observed an apparent wettability shift due to hysteresis and a capillary pressure barrier linked to pore-wall slope variations. Simulations replicated experimental trends, confirming the role of wettability in pore-scale displacement. These findings provide critical insights for improving pore-network models and understanding wettability effects in porous media.

* Corresponding author.
E-mail address: johannes.mueller@itlr.uni-stuttgart.de (J.C. Müller).
[1] These authors contributed equally to this work as co-first authors.

https://doi.org/10.1016/j.jcis.2025.137884
Received 31 January 2025; Received in revised form 30 April 2025; Accepted 13 May 2025
Available online 16 May 2025

1. Introduction

Two-phase flow in porous media is widespread in natural processes, such as part of the global water cycle [1] and is used in various industrial technologies, including textile technology, inkjet printing [2], fuel cell application [3], CO_2 sequestration [4], enhanced oil recovery [5] or contaminant hydrology [6]. To enable the calculation of large-scale (Darcy-scale) systems, macroscopic modelling approaches are usually used which are based on averaging over a representative elementary volume [7,8]. These approaches need closure relations, which depend on pore-scale dynamics. The challenge is to link the macroscopic models explicitly with the pore-scale effects in a systematic way [9,10]. To establish such a link the understanding of pore-scale effects is necessary. Considerable progress has been made in the understanding of how pore-scale effects influence global displacement patterns since the initial works. The displacement types have been characterized by Lenormand [11] in a phase diagram depending on the viscosity ratio $\mathrm{M} = \mu_i/\mu_d$ between the invading and the defending fluid and the capillary number defined as $\mathrm{Ca} = \mu u/\gamma$ with u as the characteristic velocity, μ the viscosity of the invading fluid and γ the interfacial tension relating the viscous to the capillary forces. Primkulov et al. [12] extended the phase diagram using dynamic and quasi-static pore-network models by incorporating the influence of wettability, characterized by the contact angle θ. Five main global displacement types are distinguished by the combination of $\mathrm{M} - \mathrm{Ca} - \theta$: (i) viscous fingering; (ii) stable displacement; (iii) invasion percolation; (iv) cooperative pore filling; and (v) corner flow. They demonstrated that decreasing the contact angle leads to a wettability-controlled transition from invasion percolation to cooperative pore filling and finally to corner flow.

One successful computational approach to conduct investigations on the pore-scale is pore network models (PNM) [13]. They include pore-scale information in a computationally efficient way by using closure relations which account for the fact that PNMs not fully resolve the pore space. These are relations for critical entry pressures, throat conductivities and the relationships between the pore-local capillary pressure P_c (the pressure difference between two fluids in hydrostatic equilibrium) and the wetting fluid saturation S. The currently used $P_c(S)$-relationships depend on geometrical arguments about the pore shape and physical arguments about the displacement type and they are equilibrium relationships between capillary pressure and saturation [14–17]. But when a time-resolved pressure signal is recorded for type (iii), (iv) or (v) displacement, a highly intermittent capillary pressure response occurs even for very low Ca, when the saturation is increased [18–21]. This intermittency is caused by instabilities of the fluid-fluid interface during a pore-filling when the interface encounters a variation in the cross-sectional area. This can lead even for so-called quasi-static displacements (very low Ca) to pore-scale events which are much faster than the overall process and represent a challenge for the current pore-local relations used by PNM. Such rapid movements from one stable to another stable meniscus position were first described by Haines [22] and called Haines jumps. Although the important role of pore wall wettability for these instabilities is known, quantitative data on the relation between pore-local capillary pressure and the saturation of a pore is currently limited. But to evaluate the validity and to improve pore-local relations it is needed.

One way to obtain it is through pore-resolved investigations enabled by the developments in high resolved imaging, microfluidic experiments and pore-resolved calculations. These approaches allow detailed analysis of pore-scale instabilities. Two types of studies can be distinguished: those that analyze single pore filling and those that analyze cooperative pore fillings.

For both types it is known that different boundary conditions lead to different jump velocities and pressure signatures: controlling the flow rate or sequentially increasing the inlet pressure [23,24]. Studies on single pore filling show that Haines jumps occur when capillary forces can no longer support the interface or when volume constraints cannot be met [25]. Sun and Santamaria [26] point out that jumps are more likely to occur when pronounced pore constrictions or small contact angles are present, or if the porous system is soft — due to elastic deformations, interacting menisci, or gas bubbles. The critical pore entry pressure is determined by surface tension, contact angle, and pore geometry. Hensel et al. [27] distinguish between two types of wetting transitions when the throat opens into the pore body with a sharp corner. The contact line (intersection of the interface with the wall) de-pins at the pore throat only if $\theta > \frac{\pi}{2} - \Psi$, where Ψ is the corner angle. A case referred to as Laplace breakthrough. If $\theta \le \frac{\pi}{2} - \Psi$, canthotaxis occurs, and the contact line de-pins *after* passing the throat. This behavior is also known for capillary pressure maxima in geometrically smooth geometries [28–30]. We therefore refer to the geometric divergence zone, in which the narrow constriction expands into the pore body, as the pinning *region*. As the contact line traverses this region, it may either remain completely pinned or slow down temporarily, as pressure and volume accumulate behind the increasingly curved interface. The duration for a jump was estimated by Mohanty et al. [31] by balancing capillary and inertial forces, showing it scales with fluid density and pore radius cubed, and inversely with surface tension. While the specific geometry of the pore also influences the time scale. For pores on the μm-scale, this results in durations on the order of a few milliseconds. Relaxation times observed in column-scale experiments are much longer and involve different mechanisms of subsequent fluid redistribution [32]. Schlüter et al. [33] identified even three stages ranging from seconds to hours. For cooperative pore fillings with controlled flow rate Armstrong and Berg [34] investigate pore filling instabilities in a hexagonal patterned micromodel in the transition from capillary fingering to stable displacement ($\mathrm{Ca} = 10^{-6}$ to 10^{-4}). They state that the intrinsic dynamics are governed by capillary-viscous-inertial forces influencing the interface dynamics across multiple pores depending on the local pore geometry as well as the fluid availability in adjacent pores. They highlight the aspect of cooperative filling in the sense that menisci in adjacent pores may retreat during a filling event, and that the interface velocity depends on the amount of non-wetting fluid stored in nearby liquid–liquid interfaces. Andrew et al. [35] point out that such non-local effects can influence the pattern and sequence of drainage events. A study of Moebius and Or [36] investigated the inertia dominated regime ($\mathrm{Ca} \approx 0.005$ to 0.08) and show that the consideration of dynamic contact angles, inertia and wall slope led to lower jump velocities. Zacharoudiou et al. [37] studied drainage and spontaneous imbibition in a single pore connected to multiple throats. They found that inertia must be considered when events occur below a critical Ohnesorge number ($Oh = \eta_w/\sqrt{\rho\gamma L_s}$), which relates viscous, inertial, and capillary forces. Furthermore they find that during a pore-filling event, the interface can change its shape from concave to convex even though the wall wettability remains unchanged, therefore has a constant contact angle ($\theta = const.$). This phenomenon was theoretically predicted and is related to the shape of the pore walls [38,28,29]. It is also known as capillary valve effect [39], capillary pressure barrier and was recently called wettability reverse [40]. Pavuluri et al. [41] investigated the imbibition process into a pore body and pointed exactly to the combination of contact angle and shape of the pinning region to be relevant for capillary pressure barriers and therefore determine the invasion paths as well as local pore filling relations.

In cooperative pore filling studies, sudden pressure drops can be observed in the pressure signal measured at the inlet of the experimental setup. Recently, Yiotis et al. [42] showed that for Haines jumps occurring at low capillary numbers ($\mathrm{Ca} \approx 10^{-6}$) in a micro-model filled with cylindrical posts, the Young–Laplace equation still relates the pressure monitored at the inlet of the micro-model and the curvature of the meniscus just before a jump occurs. Jang et al. [30] conduct single-pore filling experiments considering the influence of pore-wall wettability on Haines jumps at $\mathrm{Ca} \approx 10^{-7}$. They found good agreement with the modified Young–Laplace equation, which accounts for wall slope, indicating quasi-static conditions just before the onset of instabilities. However, the sudden pressure jump, occurring faster than their 250 ms sampling

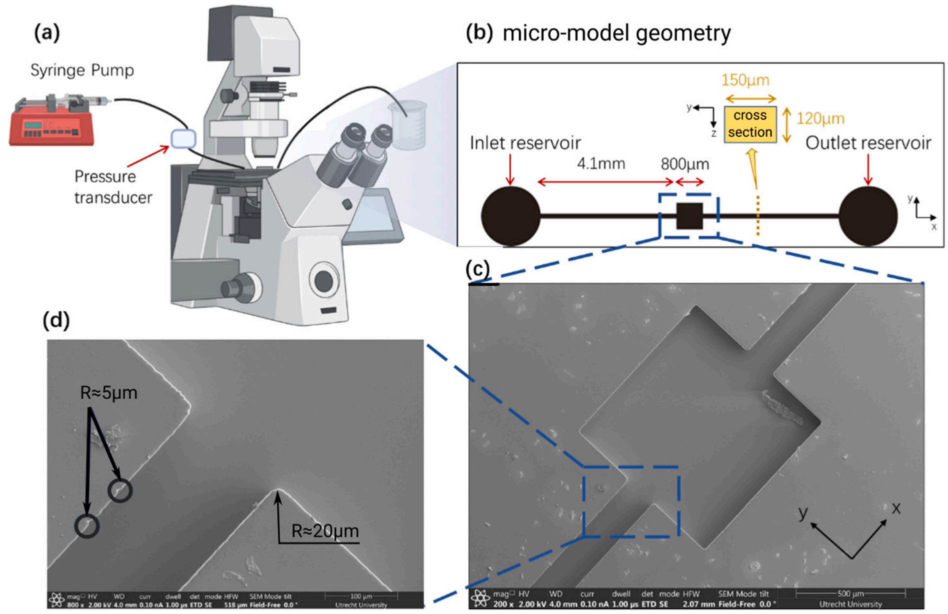

Fig. 1. Schematic of the experimental setup and details of one micro-model. a) The setup consists of a syringe pump, the pressure transducers, and the PDMS models on the piezo-driven stage of the confocal microscope. b) Top view of the micro-model geometry shown in black solid parts in the XY-plane. A cross-section of the outlet channel is shown in yellow. c) SEM imaging of the pore area. d) Zoomed part of the inlet channel opening into the pore. The corners are not sharp but have a radius of $\approx 20\,\mu$m. Two obvious cavities with around $5\,\mu$m depth are highlighted with circles.

interval, was underestimated. This observation is consistent with the findings of Sun and Santamaria [26].

Linking the measured pressure drops to interface curvature and the position of the contact line in the pinning region remains challenging due to limited spatial resolution. This limits the investigation of the influence of pore wall wettability and pore geometry in the pinning region.

The aim of this article is to investigate the role of intrinsic surface wettability on interface instabilities to obtain quantitative data which can be used to revisit and improve existing pore-filling relations for PNMs. We investigate single pore fillings with a high resolution of the pinning region - since this region determines the pore entry pressure. By controlling the flow rate, we can control the available fluid volume for the pore filling and slow down interface dynamics such that transient interfacial shapes can be captured. This allows us to directly observe the transition from quasi-static to dynamic interface motion with respect to apparent wettability changes due to geometry and velocity and their influence on pore entry pressures, interfacial dynamics and pore-local $P_c(S)$-relationships.

Two displacements are studied in the polydimethylsiloxane (PDMS) micromodels: water displacing air and water displacing Fluorinert for a variation of three different injection velocities (Ca = 2.57×10^{-6} to 1.68×10^{-4}). The pore wall wettability was varied by introducing functional chemical groups, changing the contact angle to $\theta = 60°, 95°, 120°$ for water in air. The experimental setup and procedure as well as the wettability modification of the micro-model is described in Section 2. Furthermore, the experiments are complemented by pore-resolved numerical computations using a reduced order level-set method introduced in Section 3. The image processing and the synchronization with the pressure signal allow us to associate the interface position and curvature with the corresponding recorded pressure as discussed in Section 4. Section 5 presents a comparison between the numerical and experimental results.

2. Experimental setup and methodology

The schematic of the experimental setup is shown in Fig. 1a). To investigate the movement and curvature of the two-phase interface in our microfluidic experiments a Nikon A1+ confocal laser scanning microscope (CLSM) was utilized. A micro-model was placed on the piezo-driven stage of the confocal microscope. A syringe pump (Harvard Apparatus 1 Pico Plus Elite Programmable Syringe Pump) provided a constant injection velocity. The accuracy of the injected flow rate was qualified in [49] with a standard deviation of ± 0.04 mm/s for the mean flow velocity. The pump and the inlet of the micro-model were connected with a plastic tube of 0.8 mm inner diameter while another plastic tube connected the outlet of the micro-model to the atmosphere. Additionally, a Fiber Optic Pressure Sensor (FOP-M260) was embedded in the inlet plastic tube, allowing us to acquire pressure changes in the fluid used to fill the micro-model with a temporal resolution of 62.5 Hz. The operating range is from -40 kPa up to 40 kPa relative to atmospheric pressure with a resolution of 13 Pa. In combination with the signal conditioning module SKR manufactured by FISO Technologies Inc. the pressure acquisition system has an uncertainty of ± 200 Pa including reproducibility [43]. Before activating the syringe pump and starting pressure recording, a pressure offset was set to $\Delta p = p_{\mathrm{abs}} - p_{\mathrm{atm}} - p_{\mathrm{cin}}$ where Δp is the recorded pressure, p_{abs} is the absolute pressure, p_{atm} is the atmospheric pressure and p_{cin} is the capillary pressure of the meniscus in the inlet tubing. Before starting the syringe pump $\Delta p = p_0 = 0$. More details of the transducer's structure and monitoring setup can be found in [44] and [45].

2.1. Micro-model geometry

The micro-models were prepared from PDMS (polydimethylsiloxane) using the standard procedures of the soft-lithography technique. More details of the manufacturing process can be found in [46–48]. We designed the mask using *AutoCAD* and formed the silicon wafer with an inverted micro-model. After curing, warming, and bonding the PDMS pieces, a single micro-model was fabricated. The geometry consists of two channels each 4.1 mm in length and 150 μm in width, connected to an $800 \times 800\,\mu\mathrm{m}^2$ square pore (see Fig. 1b)). The height of the entire model was constant at $h = 120\,\mu$m. Two reservoirs with a diameter of 2 mm were placed at the beginning and end of the horizontal channels to connect the inlet and outlet tubing. The entire pore body and parts of the channels were examined using scanning electron microscopy (SEM). As shown in Fig. 1d), the side walls of the micro-model had maximal bumps or cavities up to $\pm 5\,\mu$m due to variations during the soft-lithography process [49]. The top and bottom walls showed no such roughness.

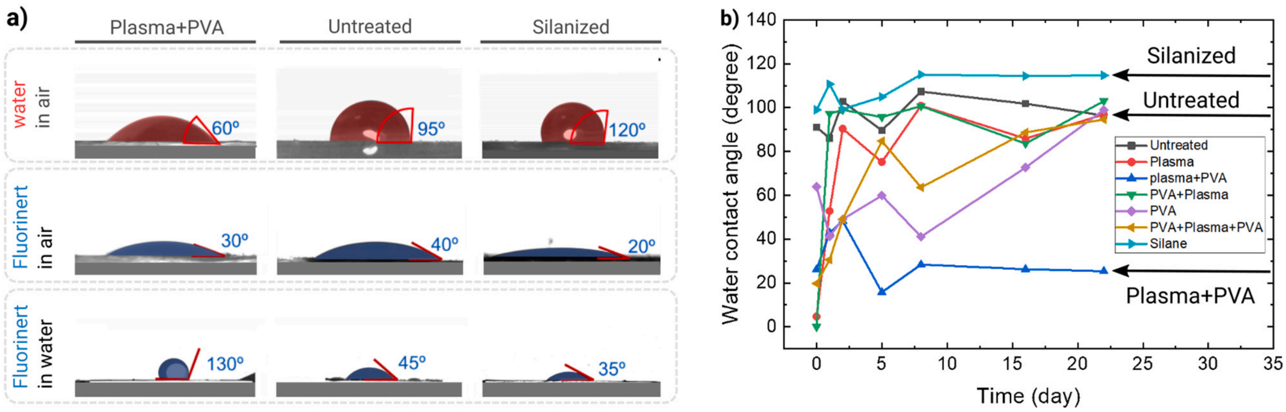

Fig. 2. a) Measured static contact angles for different PDMS treatments (columns) and for water in air, Fluorinert in air, and Fluorinert in water (rows). **b) Change of wettability over time for different treatments.** Three types of PDMS wettability (Plasma+PVA, 30°; untreated, 95° and Silanized, 120°) can maintain the wettability for at least 22 days and have been selected for our experiments. Note that the Plasma+PVA treatment renders the different wettabilities to the samples via various power of plasma treatments. Therefore, the sample marked with a 30° of water contact angle had a more powerful plasma coating on the surface than the one used for the actual displacement experiment (60° contact angle).

2.2. Wettability fabrication of the micro-model

The untreated PDMS surface exhibits hydrophobic properties ($\theta \approx 108°$). Therefore, Fluorinert-FC 43 (99+% purity) is chosen as the wetting phase, while pure water serves as the non-wetting phase. According to the supplier, Fluorinert has a viscosity of $\mu_f = 4.7$ mPa $\cdot$ s and a density of $\rho_f = 1860$ kg/m^3. For the dyed water we use $\mu_w = 1.0$ mPa $\cdot$ s and $\rho_w = 1000$ kg/m^3. The interfacial tension between Fluorinert and water is taken to be $\gamma = 55$ mN/m. All the chemicals are purchased from Sigma-Aldrich company. To modify the PDMS wettability, we combined physical and chemical approaches as described in [50,51]. After fabrication, the PDMS surface was altered to be either hydrophilic or hydrophobic by introducing functional chemical groups (such as silanol groups Si-OH, alcoholic hydroxyls C-OH, and carboxylic acids COOH) on the surface. The hydrophilic micro-model was modified through oxygen plasma treatment and a coating of polyvinyl alcohol (PVA, 99+% purity). A 1 wt% PVA solution was prepared by mixing PVA powder in deionized water and stirring for 24 hours at $60\,°C$, then cooling it until it reached room temperature. The oxygen plasma treatment was completed using the 2.6-liter plasma lab system Zepto (Diener electronic). This oxidation created sufficient hydroxyl and carboxyl functional groups on the surface for optimal bonding strength and surface wettability. The bonded PDMS was placed in an oven at $60\,°C$ for 30 minutes to achieve permanent adhesive bonding with a water contact angle of approximately 30°. After PVA coating, the wettability was maintained with a 60° contact angle for at least 20 days.

To obtain a hydrophobic surface, a silanization method is used. A silanization solution is prepared by mixing trichloro-(1H,1H,2H,2H-perfluorooctyl) silane (99+% purity) in ethanol at a volume ratio of 1:10. The mixed solution is injected into the micro-model for about 5 seconds. Two injection cycles of pure ethanol and deionized water are used to flush out the residual silane solution. The hydrophobic micro-model is dehydrated in an oven at 60 °C overnight. We have identified that preventing changes in wettability is crucial for ensuring the reproducibility of the experiments, and we have analyzed this aspect in the context of wettability changes over time for the different treatments. To evaluate the wettability modification over time, we measured the static contact angles using the sessile drop method for water droplets in air on three PDMS pieces ($20 \times 20 \times 2$ mm^3) which were treated similarly to the micro-models on consecutive days. The results are shown in Fig. 2a) for the treatments used in the actual experiments. Furthermore, Fig. 2b) presents an investigation into the durability of the wettability. The results show that the three modifications we finally chose: plasma+PVA, untreated, and silanized can maintain their wettability over days. We note that after the durability test, the treatment procedures were adjusted to enhance their effect and achieve the wettability values presented in Fig. 2a). There, we also present measurements for different surfaces and compare them to a water drop in air, a Fluorinert drop in air, and a Fluorinert drop in water. Notably, in a water environment, Fluorinert displays as the non-wetting phase on plasma+PVA coated PDMS surfaces while showing as wetting phase on untreated and silanized samples. This indicates that the hydrophilic modification maintains well on the surface for experiments involving water-Fluorinert displacement.

2.3. Fluorescence imaging

To visualize small amounts of fluid, such as thin films, fluorescein sodium salt (99+% purity) was used to dye the water for fluorescence recovery. Confocal microscopy can observe the dyed water using a 488 nm laser. Resonant scanning mirrors capture images at 30 frames per second. One fluorescent image and the camera image are simultaneously recorded. Images were captured using a 10× microscope objective with a view domain of 1.27×1.27 mm^2 and a resolution of 512×512 pixels, providing a lateral (XY) scan resolution of 2.48 μm/pixel. The fluorescent signal causes the dyed water to appear green, optimizing imaging parameters that clearly distinguish between the water and Fluorinert, resulting in a clear visualization of the two-phase interface. In the camera image, Fluorinert appears colorless while the dyed water shows as light gray.

2.4. Experimental procedure

The experiments involved two viscosity ratios: For water displacing air $M_{wa} = \mu_w/\mu_a = 55.56$, and for water displacing Fluorinert $M_{wf} = \mu_w/\mu_f = 0.2$. For each viscosity ratio, three flow rates were investigated. With syringe pump injection rates of Q1, Q2 and Q3 at 0.01, 0.1, and 0.5 ml/h. For each combination of viscosity ratio and flow rate, three micromodel wall wettabilities were used, characterized by the static contact angles $\theta_{S,WA} = 60°, 95°, 120°$ for water in air and $\theta_{S,WF} = 50°, 135°, 145°$ for water on Fluorinert, for a total of 18 experiments. The procedure for each experiment was as follows: Initially, the micro-model was saturated with air or Fluorinert, which was then displaced by dyed water. Capillary numbers were calculated as $\mathrm{Ca} = \frac{\mu U_m}{\gamma}$, where U_m is the mean velocity in the micro-channel. For water-air displacement, this resulted in capillary numbers of 2.57×10^{-6}, 2.57×10^{-5} and 1.28×10^{-4}. Respectively for water-Fluorinert displacement the numbers were 3.37×10^{-6}, 3.37×10^{-5} and 1.68×10^{-4}. According to the Lenormand diagram extended by the influence of wettability [12], these numbers place the experiments in the transition from capillary-to viscosity-dominated flow. For hydrophilic ($\theta = 60°$) and hydrophobic ($\theta = 120°$) PDMS surfaces capillary-dominated flows are expected at higher Ca numbers compared to $\theta = 95°$.

3. Numerical modelling

To complement the microfluidic experiments, numerical simulations were conducted based on the level-set method (LSM) introduced by Olsson and Kreiss [52] and implemented in *COMSOL Multiphysics 5.4* [53]. A model reduction was introduced to obtain a 2D level set model which is described in detail in the supplementary material. This approach allowed us to capture the fluid-fluid interface during the pore-filling event. The numerical domain is depicted in the Supplementary file. The geometry is set to a 2D x-axis symmetric shape. Our region of interest is the pressure and saturation variation in the pore body. The modelling geometry consists of a $400 \times 75\,\mu m^2$ rectangular inlet channel, which opens into a rectangular pore body of $800 \times 400\,\mu m^2$. This is followed by an outlet channel of $600 \times 75\,\mu m^2$. To complement the experimental investigation, we simulate the drainage process of water-Fluorinert displacement, as larger viscous pressure losses are expected here. Consequently, the curvature of the interface can no longer be directly related to the Young-Laplace equation with the pressure measured at the inlet tubing of the experiment.

3.1. Initial condition and wall boundary conditions

The initial phase distribution is set as follows: In the inlet channel, the level set variable for water, $\phi = 1$, is set in a $100 \times 75\,\mu m^2$ rectangular area. The rest of the computational domain is fully saturated with the level set variable for Fluorinert, $\phi = 0$. This setup allows the initial meniscus curvature to develop. Special care must be taken to include the effect of fluid adhesion to the wall. The approach chosen here is based on the formulation of uncompensated Youngs stress [54,55] to improve surface tension force calculations of $F_{\text{st-2D}}$ near the contact line by allowing smoother interface curvature calculations [56], contrasting with directly prescribing the contact angle as typically done with the volume of fluid method [57]. Therefore a boundary force of the form

$$F_{\theta-\text{num}} = \gamma\delta\left(\mathbf{n}_{\text{wall}} \cdot \mathbf{n} - \cos\theta_{\text{num}}\right)\mathbf{n} \tag{1}$$

is considered. It acts only locally near the three-phase contact line and only if the prescribed contact angle θ_{num} is not fulfilled ($\mathbf{n}_{\text{wall}} \cdot \mathbf{n} \neq \cos\theta_{\text{num}}$), thereby enforcing the prescribed contact angle θ_{num} [53]. Unlike uncompensated Youngs stress, $F_{\theta-\text{num}}$ measures in our case not the difference between actual interface orientation and static contact angle θ_S but relative to the effective angle θ_{num}. We note that θ_{num} serves as an effective contact angle for regions next to the three-phase contact-line where effects below mesh resolution are present [54,58,59]. Since θ_{num} relates to the normal of the interface as $\mathbf{n} = \mathbf{n}_w \cos(\theta_{\text{num}}) + \mathbf{n}_t \sin(\theta_{\text{num}})$, with $\mathbf{n}_w$ as the wall normal and $\mathbf{n}_t$ lying in the wall and normal to the three-phase contact line. Enforcing θ_{num} changes the local interface curvature, affecting the surface tension force near the three-phase contact line since $F_{\text{2D-st}} \sim \kappa$. The investigated PDMS surfaces exhibit static contact hysteresis, resulting in a difference between the static contact angle measured with the sessile drop method in Section 2.2 and the static advancing contact angle, denoted as $\Delta\theta = \theta_{AS} - \theta_S$. The static advancing contact angle θ_{AS} is defined as the angle just before the contact line advances [60]. For higher velocities of the contact-line, the dynamic advancing contact angle θ_{AD} is observed [61,62]. Since small contact line speeds are expected for $\text{Ca} < 5 \times 10^{-6}$ we prescribe a constant static advancing contact angle independent of the contact line velocity $\theta_{\text{num}} = \theta_{AS}$ [63]. For higher capillary numbers, we prescribe a constant dynamic advancing contact angle $\theta_{\text{num}} = \theta_{AD}$ since, as we do not anticipate significant velocity dependence of θ_{AD} for $\text{Ca} < 5 \times 10^{-4}$. The values of θ_{AS} and θ_{AD} were obtained from measurements in the microchannel for different PDMS surfaces, as described in the supplementary material. Prescribing θ_{num} as an effective angle imposes requirements on mesh resolution. Particularly for the first layer of cells next to the wall. The distance from their cell center to the wall $\Delta x/2$, is known as the cut-off length l which we choose to be larger than the "intermediate region" to allow for prescribing an effective (apparent) contact angle. The region next to the three-phase contact-line is "cut out" from the flow field to avoid singularities and resolve curvature changes of the interface down to the nanometer scale [58,64]. Furthermore, $\Delta x/2$ must be smaller than the length scale L at which other hydrodynamic forces deform the interface. Following Afkhamiś estimation, we use $L > \text{Ca}^{1/3} l_c$. Therefore, we use $\Delta x/2 = \text{Ca}^{1/3} l_c$ as an estimate for mesh resolution, with l_c as the capillary length.

The angle θ_{xz} introduced to capture unresolved curvature was always set to $\theta_{xz} = \theta_{\text{num}}$. For the momentum equation, no-slip boundary conditions are prescribed at the walls ($u = 0$). Even though a no-slip boundary condition is present in cells with a moving interface, the size of $\Delta x/2$ determines numerical slip which, allowing for movement of the contact-line.

3.2. Inlet and outlet conditions

Since the numerical domain represents only a part of the experiment, the inlet and outlet boundary conditions are not exactly known. Therefore, three different inlet boundary conditions are used and discussed below: constant inlet pressure (CIP), constant inlet velocity (CIV) and variable inlet pressure considering the flow resistance in the inlet tubing (CFR). An overview of the boundary conditions and their parameters used for the simulations is provided in Table 1.

For the CFR condition a flow resistance R_i is formulated using expressions obtained from analytical solutions for single phase flows valid for small Reynolds numbers ($\text{Re} < 1$) in different cross sections. The general form for viscous resistance reads for ducts with a rectangular cross-section is given by $R_i^r = \frac{12\mu_i L}{wh^3}\lambda_R$, where i denotes the respective fluid phase, e.g., water, Fluorinert or air, h denotes the channel depth and λ_R is the aspect ratio function used to approximate the flow rate. For $\varepsilon = h/w > 0.8$ this approximation has less than 1% error by setting $\lambda_R = 1 - 0.627\varepsilon$ [65]. For circular cross-sections the resistance is $R_i^c = \frac{8\mu_i L_t}{\pi r^4}$. For instance, the water flow resistance can be calculated by considering the water phase both in the circular inlet tubing and in the part of the rectangular micro-channel which is not resolved with the computational domain. Given the length of water in the two parts as $L_t = 25\,\text{cm}$ and $L_c = 5\,\text{mm}$, the water flow resistance used for the simulation is $R_w = \frac{12\mu_w L_c}{wh_c^3}\lambda_R + \frac{8\mu L}{\pi r_t^4}$, whereas in our case r_t is the radius of the inlet tubing and $h_c = d$ is the micro-channel depth. This formulation enables us to formulate the inlet pressure dependent on the flow rate prescribed by the syringe pump (resulting in the mean velocity U_m). Therefore, the inlet pressure is given as, $p_{\text{inlet}} = p_{\text{pump}} - U_m R_w$. The outlet pressure can be obtained by considering in addition to the viscous forces also the capillary pressure due to the Fluorinert-air interface in the outlet tubing. Therefore, the outlet pressure is $p_{\text{outlet}} = p_{\text{atm}} + U_m R_f + p_{\text{cout}}$, where p_{atm} is the atmospheric pressure and R_f is the Fluorinert flow resistance. We estimate the capillary pressure in the outlet tubing with $p_{\text{cout}} = \frac{2\gamma_{\text{fa}}}{r_{\text{min}}}$ while the minimum radius of curvature is $r_{\text{min}} = 0.4\,\text{mm}$ in the outlet tubing.

4. Experimental results of Water-Air displacement and discussion

In this section, we present the experimental results of Water-Air displacement. The results of Water-Fluorinert displacement are described in the supplementary material. We developed an automated image analysis using *ImageJ* [66], allowing us to determine the position and curvature of the interface. In each case, we begin with the influence of wettability and flow rate on saturation in Section 4.1 and then examine their impact on characteristic pressures and interface curvature in Section 4.2. Additionally, we synchronized the recorded pressure with the images, enabling us to link pressure signal characteristics to the curvature and

Table 1
Overview of boundary conditions and numerical cases.

Condition name	Boundary conditions p [Pa], $\mathbf{u}$ [m s^{-1}]	Contact angle θ_{num} [°]	Water flow resistance R_w [Pa s/m]
constant inlet pressure (CIP)	inlet: $p_{\mathrm{in}} = 600, 800, 1000, 1200$ $\nabla \mathbf{u} = 0$ outlet: $p_{\mathrm{out}} = 0$ $\nabla \mathbf{u} = 0$	120	-
constant inlet velocity (CIV)	inlet: $\nabla p = 0$ $u = 0.02, 0.05$ outlet: $p_{\mathrm{out}} = 0$ $\nabla \mathbf{u} = 0$	120	-
inlet pressure considering flow resistance (CFR)	$p_{\mathrm{in}} = p_{\mathrm{pump}} - U_m R_w$ where $p_{\mathrm{pump}} = 1000$ $p_{\mathrm{out}} = p_o + U_m R_f + p_c(f-a)$ where $p_o = 0$	0, 30, 60, 90, 120, 150, 180	8544.8
	$p_{\mathrm{in}} = p_{\mathrm{pump}} - U_m R_w$ where p_{pump} : $500, 600, 800, 1000, 1200, 1400$ $p_{\mathrm{out}} = p_o + U_m R_f + p_c(f-a)$ where $p_o = 0$	120	8544.8
	$p_{\mathrm{in}} = p_{\mathrm{pump}} - U_m R_w$ where p_{pump} : 1000 $p_{\mathrm{out}} = p_o + U_m R_f + p_c(f-a)$ where $p_o = 0$	120	$R_w = 8333\,n$ where $n \in \mathbb{N}$ and $0 \le n \le 6$

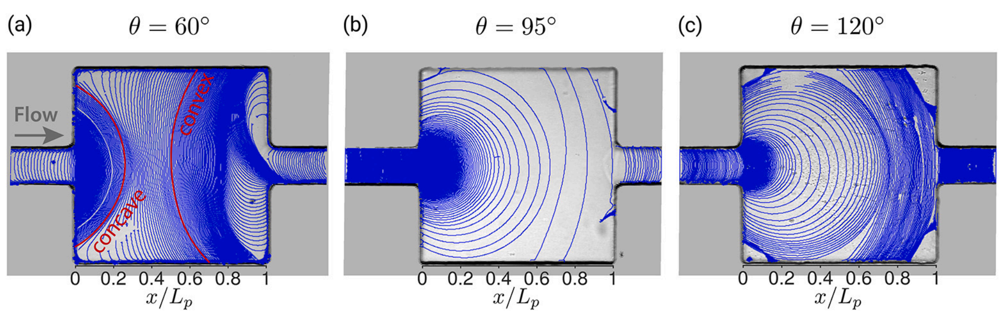

Fig. 3. Superimposition of all tracked interface positions in one image. The separation time between frames is 1/30 s. Water is displacing air from left to right with the injection flow rate Q1. The pore wall wettabilities are a) $\theta_S = 60°$, b) $\theta_S = 95°$ and c) $\theta_S = 120°$.

position of the interface which is discussed in Section 4.2. For an overall comparison both fluid displacement types are compared in Section 4.3 with respect to flow rates and final water saturations. The naming convention for the experiments is constructed from the static contact angle θ_S, the prescribed flow rate, and displacement type (e.g. 60_Q2_WA for water displacing air and 60_Q2_WF for water displacing Fluorinert).

4.1. *Influence of wettability and flow rate on saturation*

We begin by describing the influence of wettability at the lowest flow rate, Q1, during the displacement of air by water. The water-air interface was extracted from recorded images using the *ImageJ* macro *CurveTrace* [66], [67]. Fig. 3 shows the tracked interfaces in blue for three wettabilities: a) $\theta_S = 60°$, b) $\theta_S = 95°$, and c) $\theta_S = 120°$ and shows the complete field of view in the x-direction. The time interval between each recorded frame is fixed and with a value of $t = 1/30$ second. Therefore, a high density of lines indicates a slow-moving interface, while a larger distance suggests a faster movement. For all wettabilities, the meniscus slows down, when the contact line reaches the corner where the channel opens into the pore at $x/L_p = 0$. Once the fluid pressure exceeds the burst pressure, the pore fills. Quantitative values are discussed in subsequent sections. In experiments with hydrophilic treatment ($\theta_S = 60°$), the meniscus initially shows a concave shape in the micro-channel from the flow direction perspective, changing to a convex shape at the pore corner. This effect is a capillary pressure barrier known from spontaneous imbibition [41] and has been recently termed wettability reversal for forced wetting [40]. The meniscus maintains this convex shape until reaching the horizontal side walls, then reverts to a concave shape. This behavior was only observed in experiments with the lowest flow rate, highest wall wettability Q1_60_WA. Compared to other cases, this was also the only experiment where corner flows were observed ahead of the main interface and no air was trapped in the pore. In all other experiments, the interface grows like a bubble into the pore body and touches the side walls, trapping air in the corners of the pore body.

Fig. 4 illustrates water saturation over time during pore-filling for three wettabilities and flow rates Q1, Q2, and Q3. Saturation calculations consider only the pore-body volume. The evaluation considers only r_{xy} neglecting the curvature perpendicular to the observation plane (r_{xz}). Due to the quasi-2D system during the pore-filling $r_{xy} >> r_{xz}$ therefore only a minimal error is introduced. In Fig. 4 a), for the Q1 flow rate, the hydrophilic model ($\theta_S = 60°$) achieves full water saturation ($S = 100\%$) of the pore-body, while hydrophobic models result in lower final saturation values, down to $S = 92\%$ for Q1_120_WA. For the evaluation of water saturation, the uncertainty was estimated to be 2%

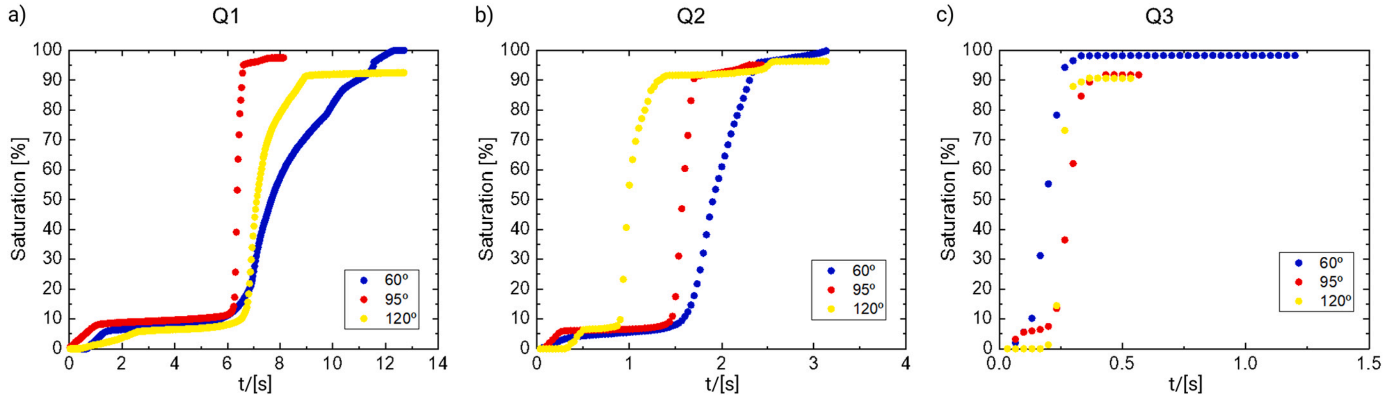

Fig. 4. Saturation of water over time during pore filling for the three wettability conditions. The different flow rates are depicted in a) for Q1, b) for Q2 and c) for Q3. (For interpretation of the colors in the figure(s), the reader is referred to the web version of this article.)

of the indicated value, accounting for measurement, post-processing, and repeatability. This trend is also observed at higher flow rates, although final saturation values are closer for the intermediate flow rate Q2, as shown in Fig. 4 b).

4.2. Interface curvature and pressure changes for the water-air displacement

In this section the relationship between interface curvature and the measured pressure is discussed. The comparison is shown in Fig. 5. Each plot provides a detailed view of the pressure curve (blue) during the time when image data is available. Corresponding to the interface passing through the confocal microscope's field of view. During this period, one component of the interface curvature, was evaluated. The mean interface curvature expressed as: $\kappa = 1/r_{xy} + 1/r_{xz}$ with r_{xy} as the principal radius of curvature in the x-y plane. This approximation holds when the interface curvature remains constant, allowing it to be represented by two inscribed circles. The radius r_{xy} was evaluated by fitting a circle to the interface which was sufficient for most image data. However, this approach was limited when the curvature was non-constant, such as during pore filling when multiple interfaces formed due to air being trapped in corners. In such cases, curvature evaluation was not possible, though the pressure curve is still presented until the interface exits the field of view. Since determining the radius of curvature required an extensive sequence of events during image acquisition and image analysis a quantitative validation of the data as evaluated for experiment 95_Q1_WA with the analytical solution of Crisp and Thorpe [38] was performed. Details are provided in the supplementary material. The resulting mean relative deviation is 1.8%. This provides evidence of the reliability of the data acquisition and post-processing. For r_{xz}, no significant changes were expected due to the constant depth of the micro-model.

The radius of curvature synchronized with the pressure signal is shown in red in Fig. 5. A key finding is that curvature changes significantly in the "pinning" region, just *before* pore filling occurs. The reference experiment (95_Q1_WA) depicted in Fig. 5 d) highlights these dynamics. The "pinning" time was identified by evaluating when the contact line reached and moved around the corner of the pore body. Since these corners are not sharp but have a radius of $R_c \sim 5.6\mu m$, we define this region as the "pinning" region. The start and end times of contact line movement within this region are marked by black vertical lines in Fig. 5 d). To simplify discussion, we drop subscripts and normalize the radius of curvature (r) by half the channel height ($r_0 = h/2$), yielding a normalized radius r/r_0. The minimal attainable radius $r/r_0 = 1$ corresponds to the maximum possible curvature, indicated by a horizontal line in all plots. During "pinning" the radius decreases to a minimum before increasing again just prior to pore entry ("burst"). This pressure increase during "pinning" represents a pore entry pressure, indicating that even when channel entry pressure is reached, it may not suffice to fill the pore. This has implications for pore-local capillary pressure-saturation relationships used in pore network models, as highlighted by Pavuluri et al. [41], who emphasized the influence of transition regions (pore-throat to pore-body). The blue pressure curve, shows that as curvature decreases, pressure rises, but slightly drops just before a major decrease associated with pore-filling.

Visual observation suggests that during "pinning" the contact line appears stationary; however, image analysis reveals slow but continuous movement a phenomenon known as *canthotaxis* [27]. This behavior was observed across experiments with flow rates Q1 and Q2, but could not be confirmed for Q3, due to the limited temporal resolution. For experiment 60_Q1_WA (Fig. 5a), distinct curvature changes were observed. Initially, while moving through the channel, the meniscus had a negative (concave) curvature. Upon reaching the "pinning" region, it transitioned from concave to convex, with r/r_0 showing a vertical asymptote as it shifted from negative infinity to positive infinity (note axis scaling). This behavior aligns with numerical results from Pavuluri et al. [41], who reported similar transitions during spontaneous imbibition near capillary barriers. After "pinning" a convex meniscus shape persisted during pore-filling ($2s < t < 6s$), followed by another transition from convex to concave within the pore body. This second transition causes r/r_0 to briefly approach positive infinity before returning from negative infinity. A sharp decrease in r/r_0 at $t = 8.45s$ corresponded to interface movement into the outlet channel. Comparing wettabilities for flow rate Q1 (first column of Fig. 5), differences in normalized radii highlight variations in apparent contact angles ($r_{xy} = \frac{h}{cos(\theta_{app})}$). For Q1, apparent contact angles correspond to static advancing angles (θ_{AS}). At higher flow rates (e.g. Q2), dynamic advancing angles (θ_{AD}) were observed instead.

4.3. Overall comparison

To compare the pore-filling processes for both fluid displacements, the changes in volumetric flow rate (Q) over injection time are shown in Fig. 6 a)-c). Both displacement types exhibit a similar trend: an initial decrease in Q when the interface reaches the pinning region, followed by a sudden increase as the burst pressure is overcome, leading to a sharp drop in resistance for the interface. The increase in Q corresponds to the drop in capillary pressure. After the pore-filling event, Q decreases again. For the same wettability and prescribed flow rate, water-air displacement demonstrates a longer pinning period before overcoming the burst pressure compared to water-Fluorinert displacement. This difference is particularly evident for Q1 at $\theta = 60°$, as shown in Fig. 6 d). Fig. 6 e) quantifies the time difference between flow rate peaks for water-air and water-Fluorinert displacements across all experiments. The largest time difference occurs at Q1, with the untreated PDMS model ($\theta = 95°$)

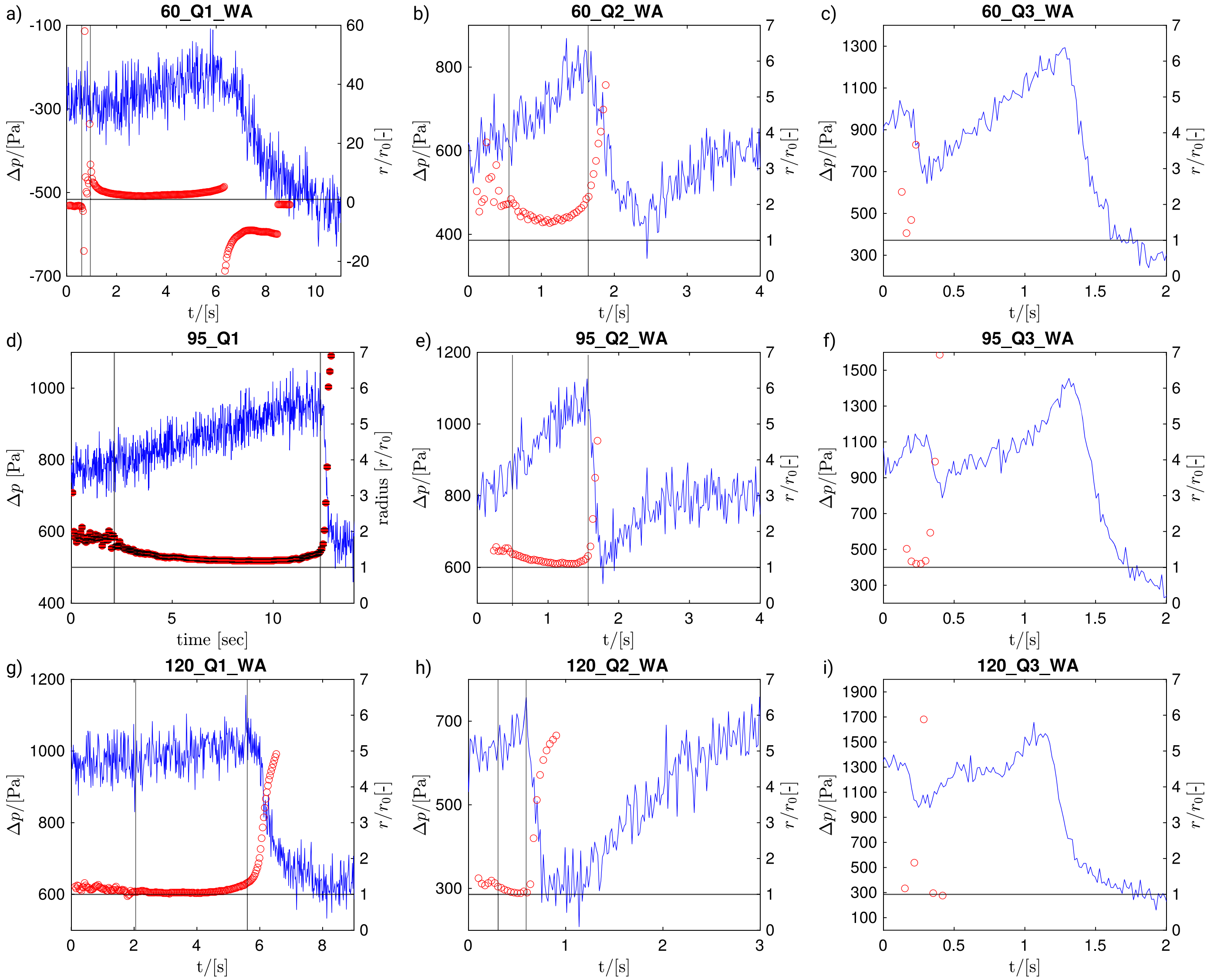

Fig. 5. Comparison of the pressure signal during the pore-filling as blue line and the normalized radius of curvature r/r_0 of the interface in red circles for all water-air displacement experiments. The wettability changes per row, while the flow rate changes per column. a) 60_Q1_WA, b) 60_Q2_WA, c) 60_Q3_WA, d) 95_Q1_WA, e) 95_Q2_WA, f) 95_Q3_WA, g) 120_Q1_WA, h) 120_Q2_WA, i) 120_Q3_WA. The radius of curvature is normalized with half the height of the micro-channel $r_0 = h/2$. The vertical black lines indicate the start and end of the "pinning" time. The horizontal black line is the minimal attainable positive radius of curvature. We have indicated error bars for the radius of curvature in graph d). Since it is in the size if the graph point size we have omitted it in the other graphs.

showing the longest delay. This suggests that the water-air interface requires more time to overcome the "pinning" region. Despite a constant mass flow rate being prescribed by the syringe pump, this is not reflected in the evaluated volumetric flow rate, indicating potential density or cross-sectional changes. Since deformation of the micro-model is unlikely at these flow rates [68], it is hypothesized that a small air bubble trapped near the pressure sensor inlet may cause density variations, leading to discrepancies between prescribed mass flow rates and evaluated volumetric flow rates. The observed pinning times and instabilities could therefore be related to the discussion of entrapped gas bubbles by Sun and Santamaria [26].

Fig. 6 g) compares final water saturation for different capillary numbers and wettabilities for both displacement types. Water-air displacement consistently results in higher final water saturation than water-Fluorinert displacement across all wettability conditions. For both viscosity ratios, final water saturation decreases with increasing capillary number, with a more pronounced drop between Q1 and Q2 than between Q2 and Q3.

5. Numerical results and discussion

5.1. Influence of wettability on interface curvature and phase distribution

To investigate the influence of prescribed apparent wettability θ_{num}, simulations were conducted across seven wettability conditions θ_{num}: 0, 30, 60, 90, 120, 150, 180. All simulations employed the CFR boundary condition with an injection pressure of 1000 Pa. The naming convention CFR-1000-0-WF was used to indicate the injection pressure, apparent contact angle, and the displacement type (WF for water displacing Fluorinert). The resulting fluid distributions during pore-filling are shown in Fig. 7. The first notable influence of wettability is observed in the "pinning" region. As shown in the second column, of Fig. 7, the capillary pressure barrier caused by pore geometry results in a convex meniscus for all simulations, even for $\theta_{num} < 90°$. This finding has significant implications: although a surface may be characterized as hydrophilic (e.g. $\theta_{num} = 60°$), the slope if the pore walls and the contact angle in the wall normal coordinate system (θ_{num}) determine the interface cur-

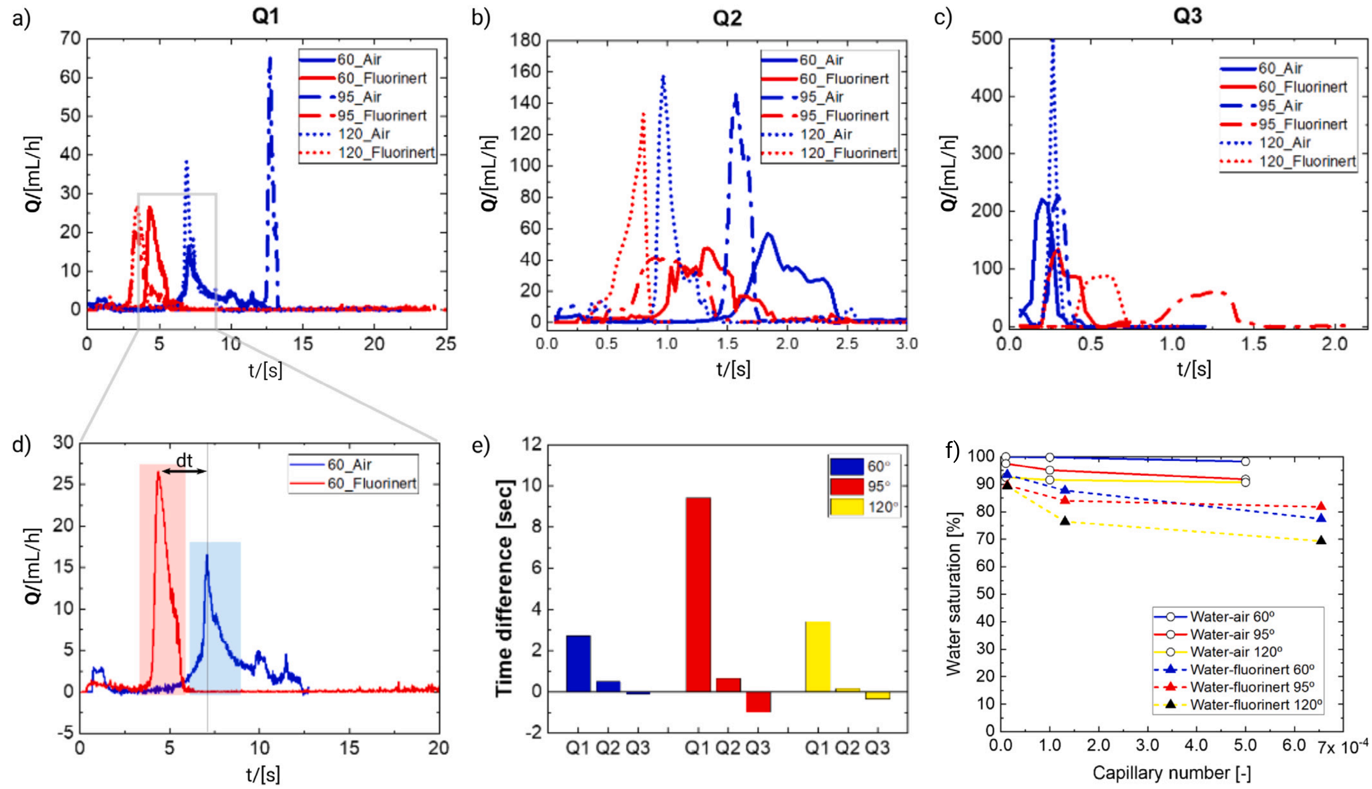

Fig. 6. Evaluated flow rate changes during injection time. Compared are in a) all cases for the injection flow rate Q1, in b) for Q2 and in c) for Q3. In d) the two viscosity ratios M are compared for the same wettability condition ($\theta = 60°$) and the same injection flow rate Q1. The blue line represents the water-air displacement with $M_{wa} = 55.56$ and the red line the water-Fluorinert displacement with $M_{wf} = 0.2$. The shadowed regions indicate the suddenly appearing flow rate peaks induced by the breakthrough of the invading phase overcoming the "pinning" region. Statistics of the time difference dt between the two peaks of the displacement types are shown in e). A positive value means the pinning period in water-air flooding is longer than that in water-Fluorinert flooding, and vice versa. f) Comparison of final water saturations for different capillary numbers and wettabilities. (For interpretation of the colors in the figure(s), the reader is referred to the web version of this article.)

vature and whether it is positive or negative. While the contact angle remains constant in the wall normal coordinate system as prescribed by the numerical boundary condition, changes in wall slope alter the interface curvature and associated apparent contact angle. Consequently, water remains the wetting phase in the wall normal coordinate system, but transitions from hydrophilic to hydrophobic behavior globally as interface curvature shifts from concave to convex. The second effect of wettability is related to pore-body filling. For $\theta_{num} < 90°$, the pore-body is completely filled with water. However, for $\theta_{num} \geq 90°$, Fluorinert becomes trapped in the corners of the pore-body.

5.2. Validation of numerical modelling

Finally we present the comparison of the numerical results with the experimental data. We start with a comparison of the phase distributions for different wall wettability in Fig. 8. Since no apparent wettability of $\theta_{app} < 90°$ was observed in water-Fluorinert experiments, an additional simulation for *water-air* displacement was conducted with $\theta_{num} = 60°$ to compare apparent hydrophilic wettability between experiment and simulation. The comparison to experiment 60_Q1_WA is depicted in Fig. 8 a), showing that the simulation accurately predicts the transition from concave to convex interface shape when overcoming the "pinning" region and during pore filling. For two apparent hydrophobic wettabilities $\theta_{num} = 135°$ and 150° the *water-Fluorinert* displacement is shown in Fig. 8 b) and c). While initial an final phase distributions agree well, slight differences occur just after de-pinning from the "pinning" region. In Fig. 8 c), the simulation shows the interface still pinned, whereas it has advanced into the pore in the experiment. This discrepancy may be due to numerical interface width ϵ needing to match the micro-model's corner radius R, as discussed in the supplementary material. Comparing time scales between experimental and numerical data, reveals slower pore-filling in experiments than simulations, likely due to non-constant volumetric flow rates caused by a trapped gas bubble in the experimental setup. The prescribed numerical contact angle represents an effective contact angle corresponding to apparent contact angles influenced by static hysteresis or dynamic effects (capillary number Ca and viscosity ratio M). Our wettability classification is based on static contact angle, θ_S, indicated alongside effective contact angles θ_A or θ_{AD} prescribed as θ_{num} for simulations.

Finally, we compare experimental pressure differences Δp with simulated differences Δp_g for experiment 95_Q1_WF and simulation CFR-1000-120-WF (Fig. 9). Due to time scale mismatches, time is normalized with t_{out}, when the interface exits the pore $t/t_{out} = 1$. Before burst pressure is overcome at $t = 0$, simulation pressure builds up while it has already done so experimentally. The pressure drop during pore-filling shows a similar trend, but with an offset of approximately 200 Pa.

This could be explained by the inaccurate representation of the second principal radius of curvature, which is estimated as $\kappa_{xz} = -\frac{2}{h}\cos(\theta_{xz})$. For the numerical setup we had assumed the advancing contact angle on the top and bottom walls θ_{xz} to be the same as on the side walls because a direct observation was not possible. Adjusting the contact angle from $\theta_{xz} = 120°$ to $\theta_{xz} = 136°$ in the closure term for the capillary forces in the third dimension of the numerical model could account for this discrepancy. Such discrepancies between the advancing contact angle on the top and bottom walls compared to the side walls could arise from the fact that advancing contact angles on rough surfaces are generally higher [63]. However, this cannot explain our case, since the side walls are considered rougher than the top and bottom

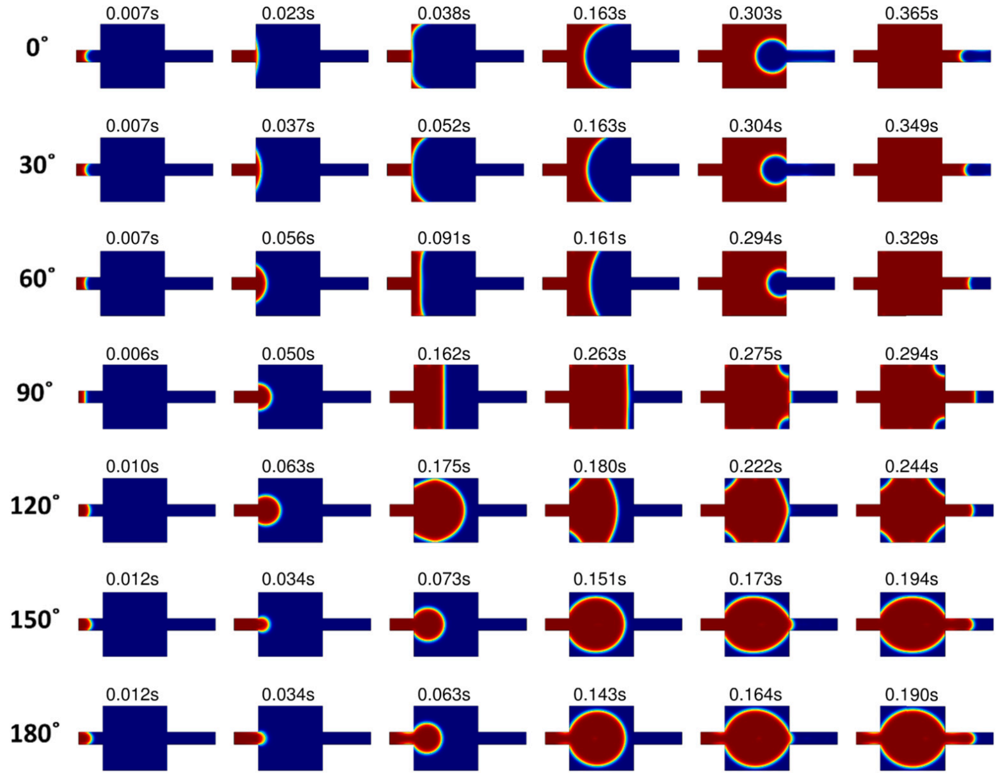

Fig. 7. Comparison of the water-Fluorinert distribution during the pore-filling for different apparent wall wettabilities θ_{num}. Flow from left to right with water in red and Fluorinert in blue. (For interpretation of the colors in the figure(s), the reader is referred to the web version of this article.)

walls. Therefore, we attribute the constant offset to an additional flow resistance in the microfluidic setup, which could originate, for instance, from a resistance at the connections between the micro-model and the reservoirs, as observed in [69].

Pressure changes appear clearer in simulations when interfaces touch pore walls (at $t = 0.75$ and $t = 1$), not observed experimentally due to viscous delays and higher temporal resolution in simulations ($\Delta t = 0.001$) resolving these changes. In the outlet regions, the simulated pressure differences decrease, while the experimental data show an increase as the interfaces in the simulations approach the outlet conditions.

6. Conclusion

This study investigated the effect of intrinsic wettability ranging from hydrophilic ($\theta_S = 60°$) to hydrophobic ($\theta_S = 95°, 120°$), on the movement of an interface into a pore-body. Using a PDMS micro-model to represent pore geometry, experiments were conducted at three different flow rates spanning the transition from capillary-dominated to viscous-dominated flow regimes. Additionally, two viscosity ratios were studied. By synchronizing pressure and image data, we linked characteristic pressure changes to interface position and curvature. Our findings reveal that instead of the intrinsic wettability θ_S the surface of the micromodel is characterized by the *static advancing* contact angle θ_{AS} since it shows a contact angle hysteresis [60,70]. While the static advancing contact angle θ_{AS} is observed for small capillary numbers (2.57×10^{-6}) and hydrophobic surfaces, no hysteresis was present for the hydrophilic case were the intrinsic wettability θ_S was observed. Furthermore, apparent wettability changes occur for higher capillary numbers (2.57×10^{-5} and 1.28×10^{-4}) due to a *dynamic advancing* contact angle θ_{AD}. This leads to the fact that a surface with an intrinsic hydrophilic wettability appears as an apparently hydrophobic surface as predicted by the Cox–Voinov relation [71,72].

Image analysis allowed us to evaluate interface curvature in the pinning region and during pore-filling events. For hydrophobic cases, the curvature of the interface was always positive, while this was not the case for the hydrophilic surface in combination with small flow rates ($\mathrm{Ca} = 2.57 \times 10^{-6}$, water displacing air). A transition form concave to convex in the pinning region and a transition form convex to concave in the pore-body was observed. In the pinning region, an *additional* apparent wettability effect was identified. Although the intrinsic contact angle (θ_S) remains constant in a wall-normal coordinate system, changes in wall slope alter the apparent contact angle in the global coordinate system and therefore the interface curvature [27]. We also identified, that in the "pinning" region, the interface exhibits slow movement associated with the breakthrough mechanism of canthotaxis. This creates a capillary pressure barrier with corresponding pore-entry pressures influenced by corner radius and intrinsic wettability (θ_S). Therefore the use of apparent wettabilities to describe the curvature of the interface and the capillary pressure is needed in pore-local relations used in PNMs. Furthermore the effect of a pore-entry pressure which can be higher than the throat entry pressure has been quantified and can now be considered in entry pressure formulations. Experimental data provided values for interface curvatures and burst pressures, showing that hydrophobic surfaces require higher burst pressures to overcome capillary barriers than hydrophilic surfaces, though such barriers are present in both cases. Water saturation analysis demonstrated that lower injection velocities lead to higher water saturations under hydrophilic conditions, while increased velocities reduce wettability effects, particularly in hydrophobic scenarios. The evaluation of the volumetric flow rate showed a mismatch to the prescribed mass flow rate, which we attribute to a small gas bubble trapped near the pressure sensor inlet. This trapped bubble not only alters the effective density but can also lead to the observed pinning times and induce interface instabilities. Future work could compare our experimental pressure-time data with Sun and Santamaria's analytical model, which considers the effects of gas bubbles on capillary pressure, and possibly extend it with a dynamic contact angle model. Since we have controlled the flow rate and therefore the available volume we limit the velocity of the Haines jump. This enabled an observation from quasi-static to dynamic interface shapes and differentiates our work with respect to the observed millisecond time scale

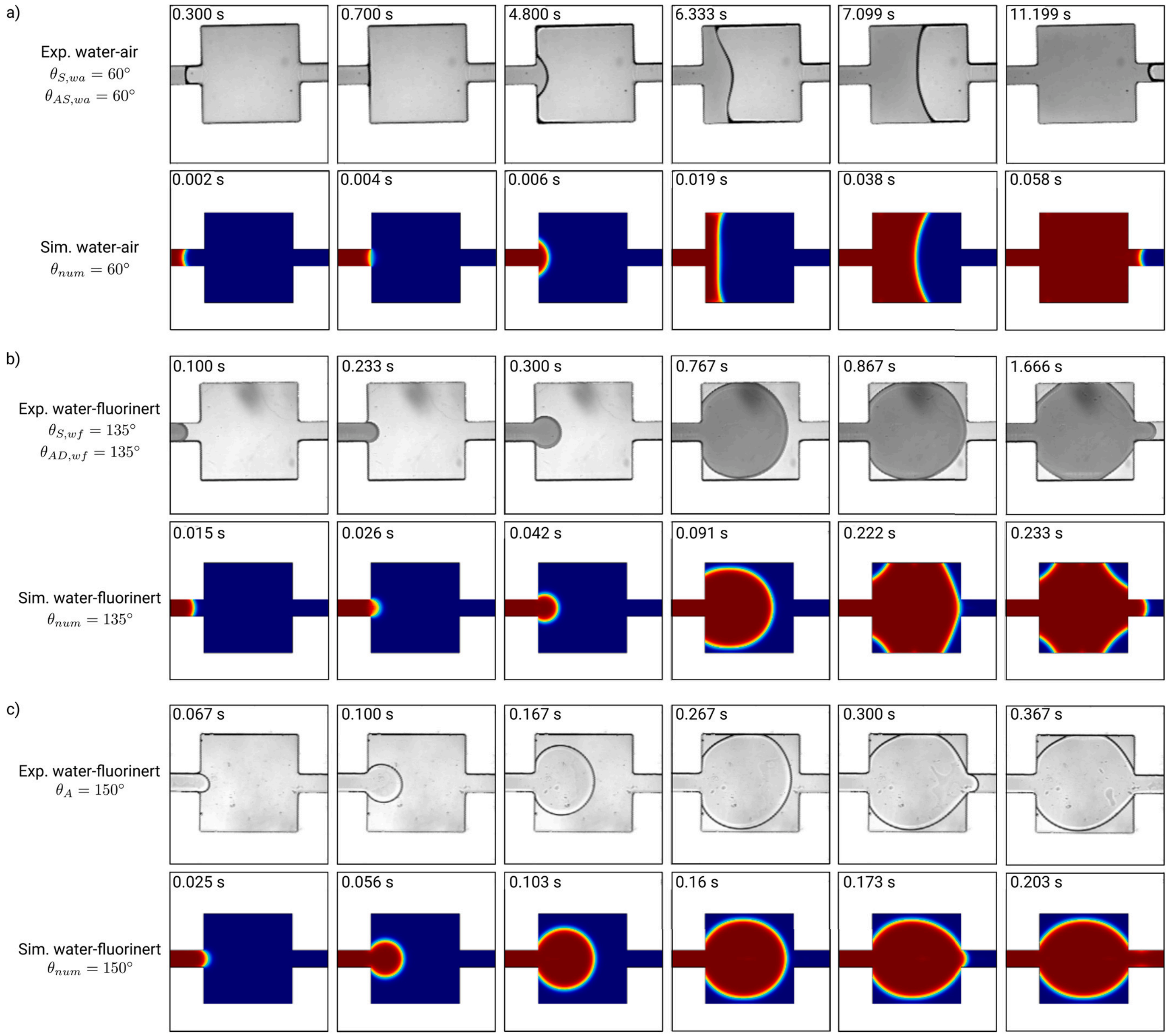

Fig. 8. Comparison of phase distributions between selected experiments and simulations during the pore filling for flow rate Q1. To show the influence of the pore geometry on the interface curvature for advancing contact angles ranging from wetting to non-wetting we have included experiment Q1_60_WA where water is displacing air in **a)** which is the only experiment with an wetting advancing contact angle $\theta_A = 60°$. The other two comparisons show water displacing Fluorinert with $\theta_A = 135°$ **b)** and $\theta_A = 150°$ **c)**. In the experimental images, water is the invading phase shown in darker gray, while the other phases, e.g., air and Fluorinert, are transparent. In the simulation results water is shown in red, and air respectively Fluorinert in blue. Flow from left to right. Since our classification of wettability is based on the static contact angle, θ_S is also indicated for the respective experiment.

from studies where much faster pressure responses have been observed due to the use of higher flow rates, cooperative fillings where mass can be provided by other fluid-fluid interfaces or due to the use of pressure boundary conditions [31,30,34,33].

The experimental investigation was complemented by simulations based on a dimensional reduced level set method which considers the aspect ratio of the micro-model inlet channel. To recompute the experiments in a reduced numerical domain different numerical boundary conditions for the channel inlet and outlet have been compared and the condition which considers the flow resistance (CFR) in the unresolved part of the experiment was chosen. When prescribing the apparent wettability in the numerical computations the changes in curvature as observed in the experiment could be captured. The comparison between numerical and experimental data with respect to the prediction of the time scale and the obtained pressure values remains challenging. This was also observed in other studies [73–75,42]. In our study we attribute the discrepancy to different effects. Firstly, the compression of small air bubbles within the inlet tubing can change the volumetric flow rate. Secondly, the applied boundary condition accounting for flow resistance (CFR) currently only considers resistance contributions from the inlet and outlet tubing. However, additional resistances arising from the connections between the tubing and the micromodel are yet not included. These resistances can significantly affect the pressure drop and should be introduced into the boundary condition. This would allow a calibration of the CFR condition specific to the microfluidic setup and dependent on the applied flow rate, particularly in the transition regime from capillary-dominated to viscous-dominated flow. Thirdly to additional dissipation mechanisms which are currently neglected in our model. These may occur due to the roughness of the vertical micro-model walls, especially for the investigated low capillary num-

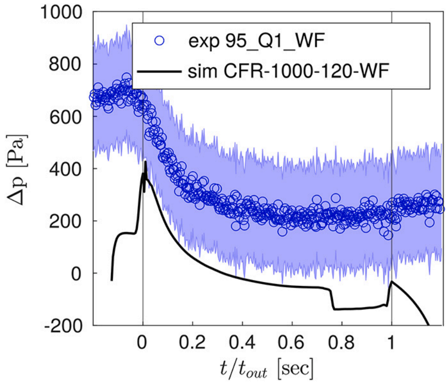

Fig. 9. Comparison of the total pressure difference Δp_g recorded from the experiment (blue circle) with the pressure difference obtained from the simulation (black line). The pressure measurements system accuracy as provided by the manufacturer [43], with a value of ± 200 Pa is indicated with a blue line.

bers leading to a stick-slip motion of the interface [76–78]. Considering these effects can be a next step in the development of the reduced level set method and the experimental design. The obtained pressure signals can now be compared to currently used pore-local $P_c - S$-relationships and used to improve them with respect to the influence of wettability. Furthermore the present work can contribute to the understanding of the interplay between the different apparent wettabilities involved in a pore-filling event which we have identified and differentiated.

CRediT authorship contribution statement

Lifei Yan: Writing – original draft, Methodology, Investigation, Formal analysis, Data curation, Conceptualization. **Johannes C. Müller:** Writing – original draft, Investigation, Formal analysis, Data curation, Conceptualization. **Tycho L. van Noorden:** Methodology. **Bernhard Weigand:** Writing – review & editing, Supervision, Resources, Project administration, Funding acquisition, Conceptualization. **Amir Raoof:** Writing – review & editing, Project administration, Methodology, Funding acquisition, Data curation, Conceptualization.

Declaration of competing interest

The authors declare that they have no known competing financial interests or personal relationships that could have appeared to influence the work reported in this paper.

Acknowledgements

The authors express their gratitude to Majid Hassanizadeh, Matthijs de Winter, Enno de Vries, Cynthia Michalkowski and Rainer Helmig for their insightful discussions. They also thank Mahin Baghery for her technical support. We acknowledge funding by the German Research Foundation (DFG), within the Collaborative Research Center on Interface-Driven Multi-Field Processes in Porous Media (SFB 1313, Project No. 327154368). Additionally, the authors acknowledge the support of the Structures of Strength (SoS), the center for interdisciplinary collaborations on porous materials, for providing microfluidic materials and expertise. The constructive comments of three anonymous reviewers helped to improve the manuscript significantly.

Appendix A. Supplementary material

Supplementary material related to this article can be found online at https://doi.org/10.1016/j.jcis.2025.137884. References cited in this supplementary material are also included in the reference section of the main text [79–84].

Data availability

The raw image and pressure data is available at https://doi.org/10.18419/darus-4683. Additional data are available from the authors upon request.

References

[1] D. Or, P. Lehmann, E. Shahraeeni, N. Shokri, Advances in soil evaporation physics—a review, Vadose Zone J. 12 (4) (2013) 1–16.
[2] H. Aslannejad, S. Hassanizadeh, A. Raoof, D. de Winter, N. Tomozeiu, M.T. Van Genuchten, Characterizing the hydraulic properties of paper coating layer using fib-sem tomography and 3d pore-scale modelling, Chem. Eng. Sci. 160 (2017) 275–280.
[3] Y. Wang, S. Basu, C.-Y. Wang, Modelling two-phase flow in pem fuel cell channels, J. Power Sources 179 (2008) 603–617.
[4] L.K. Abidoye, K.J. Khudaida, D.B. Das, Geological carbon sequestration in the context of two-phase flow in porous media: a review, Crit. Rev. Environ. Sci. Technol. 45 (2015) 1105–1147.
[5] N. Morrow, J. Buckley, Improved oil recovery by low-salinity waterflooding, J. Pet. Technol. 63 (2011) 106–112.
[6] D. Zhou, M. Blunt, Effect of spreading coefficient on the distribution of light non-aqueous phase liquid in the subsurface, J. Contam. Hydrol. 25 (1997) 1–19.
[7] J. Bear, Y. Bachmat, Introduction to modeling of transport phenomena in porous media, vol. 4, Springer Science & Business Media, 2012.
[8] S. Whitaker, Flow in porous media ii: The governing equations for immiscible, two-phase flow, Transp. Porous Media 1 (1986) 105–125.
[9] W.G. Gray, C.T. Miller, Tcat analysis of capillary pressure in non-equilibrium, two-fluid-phase, porous medium systems, Adv. Water Resour. 34 (6) (2011) 770–778.
[10] S. Schlüter, S. Berg, M. Rücker, R. Armstrong, H.-J. Vogel, R. Hilfer, D. Wildenschild, Pore-scale displacement mechanisms as a source of hysteresis for two-phase flow in porous media, Water Resour. Res. 52 (2016) 2194–2205.
[11] R. Lenormand, Liquids in porous media, J. Phys. Condens. Matter 2 (S) (1990) SA79.
[12] B.K. Primkulov, A.A. Pahlavan, X. Fu, B. Zhao, C.W. MacMinn, R. Juanes, Wettability and Lenormand's diagram, J. Fluid Mech. 923 (2021) A34.
[13] B. Zhao, C.W. MacMinn, B.K. Primkulov, Y. Chen, A.J. Valocchi, J. Zhao, Q. Kang, K. Bruning, J.E. McClure, C.T. Miller, et al., Comprehensive comparison of pore-scale models for multiphase flow in porous media, Proc. Natl. Acad. Sci. 116 (28) (2019) 13799–13806.
[14] S. Bakke, P.-E. Øren, 3-d pore-scale modelling of sandstones and flow simulations in the pore networks, SPE J. 2 (02) (1997) 136–149.
[15] M. Singh, K.K. Mohanty, Dynamic modeling of drainage through three-dimensional porous materials, Chem. Eng. Sci. 58 (1) (2003) 1–18.
[16] V. Joekar-Niasar, S.M. Hassanizadeh, H. Dahle, Non-equilibrium effects in capillarity and interfacial area in two-phase flow: dynamic pore-network modelling, J. Fluid Mech. 655 (2010) 38–71.
[17] M.J. Blunt, Multiphase flow in permeable media: A pore-scale perspective, Cambridge university press, 2017.
[18] L. Furuberg, K.J. Måløy, J. Feder, Intermittent behavior in slow drainage, Phys. Rev. E 53 (1) (1996) 966.
[19] S. Berg, H. Ott, S.A. Klapp, A. Schwing, R. Neiteler, N. Brussee, A. Makurat, L. Leu, F. Enzmann, J.-O. Schwarz, et al., Real-time 3d imaging of Haines jumps in porous media flow, Proc. Natl. Acad. Sci. 110 (10) (2013) 3755–3759.
[20] F. Moebius, D. Or, Pore scale dynamics underlying the motion of drainage fronts in porous media, Water Resour. Res. 50 (11) (2014) 8441–8457.
[21] M. Moura, K.J. Måløy, E.G. Flekkøy, R. Toussaint, Verification of a dynamic scaling for the pair correlation function during the slow drainage of a porous medium, Phys. Rev. Lett. 119 (2017) 154503.
[22] W.B. Haines, Studies in the physical properties of soil. V. The hysteresis effect in capillary properties, and the modes of moisture distribution associated therewith, J. Agric. Sci. 20 (1) (1930) 97–116.
[23] M. Hilpert, C.T. Miller, W.G. Gray, Stability of a fluid–fluid interface in a biconical pore segment, J. Colloid Interface Sci. 267 (2) (2003) 397–407.
[24] M. Moura, K.J. Måløy, E.G. Flekkøy, R. Toussaint, Intermittent dynamics of slow drainage experiments in porous media: Characterization under different boundary conditions, Front. Phys. 7 (2020) 217.
[25] M. Hatipogullari, Modelling of contact lines on heterogeneous substrates: Stick-slip and contact angle hysteresis, Ph.D. thesis, Université libre de Bruxelles, Ecole polytechnique de Bruxelles – Chimie et Science des Matériaux, Bruxelles, 2020.
[26] Z. Sun, J.C. Santamarina, Haines jumps: Pore scale mechanisms, Phys. Rev. E 100 (2019) 023115.
[27] R. Hensel, R. Helbig, S. Aland, H.-G. Braun, A. Voigt, C. Neinhuis, C. Werner, Wetting resistance at its topographical limit: the benefit of mushroom and serif t structures, Langmuir 29 (4) (2013) 1100–1112.
[28] W. Purcell, Interpretation of capillary pressure data, J. Pet. Technol. 2 (08) (1950) 11–12.
[29] G. Mason, N.R. Morrow, Effect of contact angle on capillary displacement curvatures in pore throats formed by spheres, J. Colloid Interface Sci. 168 (1) (1994) 130–141.
[30] J. Jang, Z. Sun, J.C. Santamarina, Capillary pressure across a pore throat in the presence of surfactants, Water Resour. Res. 52 (12) (2016) 9586–9599.

[31] K.K. Mohanty, H.T. Davis, L. Scriven, Physics of oil entrapment in water-wet rock, SPE Reserv. Eng. 2 (01) (1987) 113–128.
[32] R.T. Armstrong, H. Ott, A. Georgiadis, M. Rücker, A. Schwing, S. Berg, Subsecond pore-scale displacement processes and relaxation dynamics in multiphase flow, Water Resour. Res. 50 (12) (2014) 9162–9176.
[33] S. Schlüter, S. Berg, T. Li, H.-J. Vogel, D. Wildenschild, Time scales of relaxation dynamics during transient conditions in two-phase flow, Water Resour. Res. 53 (6) (2017) 4709–4724.
[34] R.T. Armstrong, S. Berg, Interfacial velocities and capillary pressure gradients during haines jumps, Phys. Rev. E, Stat. Nonlinear Soft Matter Phys. 88 (4) (2013) 043010.
[35] M. Andrew, H. Menke, M.J. Blunt, B. Bijeljic, The imaging of dynamic multiphase fluid flow using synchrotron-based x-ray microtomography at reservoir conditions, Transp. Porous Media 110 (1) (2015) 1–24.
[36] F. Moebius, D. Or, Interfacial jumps and pressure bursts during fluid displacement in interacting irregular capillaries, J. Colloid Interface Sci. 377 (1) (2012) 406–415.
[37] I. Zacharoudiou, E.M. Chapman, E.S. Boek, J.P. Crawshaw, Pore-filling events in single junction micro-models with corresponding lattice Boltzmann simulations, J. Fluid Mech. 824 (2017) 550–573.
[38] D. Crisp, W. Thorpe, The water-protecting properties of insect hairs, Discuss. Faraday Soc. 3 (1948) 210–220.
[39] H. Liu, S. Sun, R. Wu, B. Wei, J. Hou, Pore-scale modeling of spontaneous imbibition in porous media using the lattice Boltzmann method, Water Resour. Res. 57 (6) (2021) e2020WR029219.
[40] G. Yang, M. Wang, Surface roughness effect on dynamic wettability in imbibition process, Comput. Fluids (2023) 105959.
[41] S. Pavuluri, J. Maes, J. Yang, M. Regaieg, A. Moncorgé, F. Doster, Towards pore network modelling of spontaneous imbibition: contact angle dependent invasion patterns and the occurrence of dynamic capillary barriers, Comput. Geosci. 24 (2020) 951–969.
[42] A. Yiotis, N. Karadimitriou, I. Zarikos, H. Steeb, Pore-scale effects during the transition from capillary-to viscosity-dominated flow dynamics within microfluidic porous-like domains, Sci. Rep. 11 (1) (2021) 3891.
[43] FISO Technologies Inc, Medical pressure monitoring product datasheet, https://fiso.com/wp-content/uploads/2022/03/MC-00263-R8-Resonetics-Pressure-Monitoring-Catalog.pdf, 2022. (Accessed 17 April 2025).
[44] I. Zarikos, S. Hassanizadeh, L. van Oosterhout, W. van Oordt, Manufacturing a micro-model with integrated fibre optic pressure sensors, Transp. Porous Media 122 (2018) 221–234.
[45] L. Yan, H. Aslannejad, S.M. Hassanizadeh, A. Raoof, Impact of water salinity differential on a crude oil droplet constrained in a capillary: Pore-scale mechanisms, Fuel 274 (2020) 117798.
[46] Y. Xia, G.M. Whitesides, Soft lithography, Annu. Rev. Mater. Sci. 28 (1998) 153–184.
[47] D.A. Chang-Yen, R.K. Eich, B.K. Gale, A monolithic pdms waveguide system fabricated using soft-lithography techniques, J. Lightwave Technol. 23 (6) (2005) 2088.
[48] N.K. Karadimitriou, Two-phase flow experimental studies in micro-models, Ph.D. thesis, UU Department of Earth Sciences, 2013.
[49] D. de Winter, K. Weishaupt, S. Scheller, S. Frey, A. Raoof, S. Hassanizadeh, R. Helmig, The complexity of porous media flow characterized in a microfluidic model based on confocal laser scanning microscopy and micro-piv, Transp. Porous Media (2020) 1–25.
[50] J. Zhou, D.A. Khodakov, A.V. Ellis, N.H. Voelcker, Surface modification for pdms-based microfluidic devices, Electrophoresis 33 (2012) 89–104.
[51] T. Trantidou, Y. Elani, E. Parsons, O. Ces, Hydrophilic surface modification of pdms for droplet microfluidics using a simple, quick, and robust method via pva deposition, Microsyst. Nanoeng. 3 (2017) 1–9.
[52] E. Olsson, G. Kreiss, A conservative level set method for two phase flow, J. Comput. Phys. 210 (1) (2005) 225–246.
[53] A.B. Comsol, CFD Module User's Guide, version 5.4 Edition, COMSOL Multiphysics®, Stockholm, 2018.
[54] Y.D. Shikhmurzaev, The moving contact line on a smooth solid surface, Int. J. Multiph. Flow 19 (4) (1993) 589–610.
[55] J.-F. Gerbeau, T. Lelievre, Generalized Navier boundary condition and geometric conservation law for surface tension, Comput. Methods Appl. Mech. Eng. 198 (5–8) (2009) 644–656.
[56] A. Esteban, P. Gomez, C. Zanzi, J. López, M. Bussmann, J. Hernandez, A contact line force model for the simulation of drop impacts on solid surfaces using volume of fluid methods, Comput. Fluids 263 (2023) 105946.
[57] X. Yin, I. Zarikos, N. Karadimitriou, A. Raoof, S. Hassanizadeh, Direct simulations of two-phase flow experiments of different geometry complexities using volume-of-fluid (vof) method, Chem. Eng. Sci. 195 (2019) 820–827.
[58] D. Bonn, J. Eggers, J. Indekeu, J. Meunier, E. Rolley, Wetting and spreading, Rev. Mod. Phys. 81 (2) (2009) 739–805.
[59] S. Afkhami, S. Zaleski, M. Bussmann, A mesh-dependent model for applying dynamic contact angles to vof simulations, J. Comput. Phys. 228 (15) (2009) 5370–5389.
[60] H.-J. Butt, J. Liu, K. Koynov, B. Straub, C. Hinduja, I. Roismann, R. Berger, X. Li, D. Vollmer, W. Steffen, et al., Contact angle hysteresis, Curr. Opin. Colloid Interface Sci. 59 (2022) 101574.
[61] R.L. Hoffman, A study of the advancing interface. I. Interface shape in liquid—gas systems, J. Colloid Interface Sci. 50 (2) (1975) 228–241.
[62] M. Fermigier, P. Jenffer, An experimental investigation of the dynamic contact angle in liquid-liquid systems, J. Colloid Interface Sci. 146 (1) (1991) 226–241.
[63] N.R. Morrow, M.D. Nguyen, Effect of interface velocity on dynamic contact angles at rough surfaces, J. Colloid Interface Sci. 89 (2) (1982) 523–531.
[64] C. Huh, L.E. Scriven, Hydrodynamic model of steady movement of a solid/liquid/fluid contact line, J. Colloid Interface Sci. 35 (1) (1971) 85–101.
[65] D. Barthès-Biesel, Microhydrodynamics and complex fluids, CRC Press, 2012.
[66] C.A. Schneider, W.S. Rasband, K.W. Eliceiri, Nih image to imagej: 25 years of image analysis, Nat. Methods 9 (2012) 671–675.
[67] E. Katrukha, Curvetrace plugin for imagej, v0.3.5, https://doi.org/10.5281/zenodo.4534721, 2021.
[68] B.S. Hardy, K. Uechi, J. Zhen, H.P. Kavehpour, The deformation of flexible pdms microchannels under a pressure driven flow, Lab Chip 9 (7) (2009) 935–938.
[69] P. Kunz, I. Zarikos, N. Karadimitriou, M. Huber, U. Nieken, S. Hassanizadeh, Study of multi-phase flow in porous media: comparison of sph simulations with micro-model experiments, Transp. Porous Media 114 (2016) 581–600.
[70] M. Hatipogullari, C. Wylock, M. Pradas, S. Kalliadasis, P. Colinet, Contact angle hysteresis in a microchannel: Statics, Phys. Rev. Fluids 4 (4) (2019) 044008.
[71] O.V. Voinov, Hydrodynamics of wetting, Fluid Dyn. 11 (5) (1976) 714–721.
[72] R. Cox, The dynamics of the spreading of liquids on a solid surface. Part 1. Viscous flow, J. Fluid Mech. 168 (1986) 169–194.
[73] T. Ramstad, C.F. Berg, K. Thompson, Pore-scale simulations of single- and two-phase flow in porous media: approaches and applications, Transp. Porous Media 130 (2019) 77–104.
[74] J.J. Cambareri, J. Fang, I.A. Bolotnov, Simulation scaling studies of reactor core two-phase flow using direct numerical simulation, Nucl. Eng. Des. 358 (2020) 110435.
[75] P. Kunz, Modeling the dynamics of partial wetting depending on the solid microstructure and applied electric potentials using the SPH method, Verlag Dr. Hut, 2020.
[76] E. Raphael, P.-G. de Gennes, Dynamics of wetting with nonideal surfaces. The single defect problem, J. Chem. Phys. 90 (12) (1989) 7577–7584.
[77] J. Joanny, M.O. Robbins, Motion of a contact line on a heterogeneous surface, J. Chem. Phys. 92 (5) (1990) 3206–3212.
[78] B.K. Primkulov, A.A. Pahlavan, L. Cueto-Felgueroso, R. Juanes, Motion of a viscous slug on heterogeneous surfaces: crossover from stick–slip to steady sliding, J. Fluid Mech. 973 (2023) A2.
[79] V. Pratt, Direct least-squares fitting of algebraic surfaces, ACM SIGGRAPH Comput. Graph. 21 (4) (1987) 145–152.
[80] H. Bruus, Theoretical microfluidics, vol. 18, Oxford university press, 2007.
[81] C.-W. Park, G. Homsy, Two-phase displacement in Hele Shaw cells: theory, J. Fluid Mech. 139 (1984) 291–308.
[82] P. Horgue, F. Augier, P. Duru, M. Prat, M. Quintard, Experimental and numerical study of two-phase flows in arrays of cylinders, Chem. Eng. Sci. 102 (2013) 335–345.
[83] F.F. Ouali, G. McHale, H. Javed, C. Trabi, N.J. Shirtcliffe, M.I. Newton, Wetting considerations in capillary rise and imbibition in closed square tubes and open rectangular cross-section channels, Microfluid. Nanofluid. 15 (2013) 309–326.
[84] J. Berthier, F. Loe-Mie, V.-M. Tran, S. Schoumacker, F. Mittler, G. Marchand, N. Sarrut, On the pinning of interfaces on micropillar edges, J. Colloid Interface Sci. 338 (1) (2009) 296–303.